Preparation of Cu/Zn Based Catalyst Precursors – Importance of Thermodynamics and Seeding

D. Guse[1], L. Warmuth[2], F. Kreißig[1], S. Pitter[2], M. Kind[1]
[1]Karlsruhe Institute of Technology, Institute of Thermal Process Engineering
[2]Karlsruhe Institute of Technology, Institute of Catalysis Research and Technology

Abstract

Aging is one of the key steps in the preparation of Cu/Zn based catalysts. An initially amorphous intermediate transforms, depending on the exact process parameters, into the wanted crystalline precursor phase zincian malachite which is characterized by a periodic arrangement of Cu and Zn atoms and proved to be advantageous for the qualities of the final catalyst. Our approach to better understand and thus control aging is twofold. For one thing, by applying a thermodynamic model based on solubility products of naturally occurring minerals and a hybrid activity coefficient model we could show that aging can be understood as a process driven by the thermodynamic equilibrium. We were able to predict the qualitative predominance of zincian malachite for the pH and temperature ranges investigated. The model also predicted the phase composition of the aged precursor as a function of the Cu/Zn ratio in the reactant solution and the Zn fraction in zincian malachite. For another thing, we could show that aging can be significantly accelerated by seeding: the aging time necessary to induce the phase transformation was reduced by 43 to 50 % for seeding mass fractions of 3 w% and from 96 min to only 8 min for 42 w%. No negative influence of seeding on the phase composition, specific surface area, molar metal ratios and the morphology of the aged precursor could be detected. Thus, we conclude that understanding aging as a thermodynamic equilibrium process will be fruitful for the further process optimization in terms of phase composition and that seeding is a potent tool to accelerate aging, presumably also on an industrial scale.

1 Introduction

Fossil resources as raw materials for the chemical and the energy industry are becoming increasingly scarce due to geological limitations and political issues. Thus, efficient chemical processes, ideally using sustainable sources, are both essential to address climate change and from an economic point of view. Methanol (MeOH), as a key material of the chemical industry [1] and a raw material for synthetic fuels [2,3], is mainly produced from non-renewable syngas (CO, H_2) [4]. Current research shows a great potential for the synthesis from CO_2 which may be won from industrial waste streams or the atmosphere and from green H_2 obtained from electrolysis by solar or wind power [5,6].

Using syngas rich in CO_2 instead of CO requires adaptation of the process parameters as well as the Cu/Zn based catalyst used to facilitate the reaction [5]. Important catalyst properties are the specific surface, the copper surface, the arrangement of Cu and Zn atoms as well as their contact and the pore size which all result from the preparation conditions [7-10]. For syngas rich in CO_2, more H_2O is formed as a by-product and the presence of ZrO_2 as a promoter seems to become more important [5,11,12]. In general, Cu/Zn based catalysts are manufactured in a process chain with the following three key steps which determine the properties of the later catalyst:

I. co-precipitation, where an amorphous precursor precipitates by mixing two aqueous reactant solutions [13-15]
II. aging, where, by keeping a temperature between typically 60 °C and 70 °C [16] in the mother liquor, the precipitate transforms into zincian malachite ($Cu_{(2-x)}Zn_x(OH)_2CO_3$), a salt containing both Cu and Zn atoms in its lattice
III. calcination, where the aged precursor decomposes into CuO and ZnO while maintaining the arrangement of Cu and Zn atoms on the nanoscale [17].

The periodic arrangement on the atomic scale is vital for the activity [8,9,17,18] and stability [19] of the catalyst. The material is then shaped, filled into the reactor and reduced to Cu/ZnO to obtain the operational catalyst. Co-precipitation pre-determines the nanostructure of the

later catalyst [20-22], but does not ensure a defined periodic arrangement of Cu and Zn atoms [13]. Only by obtaining the intermediate zincian malachite by aging, high activities, CO_x conversions and MeOH yields are achieved [23].

However, depending on the applied recipe and aging conditions, other intermediate phases may be produced which are detrimental to the catalyst properties like the mass specific surface area or the copper surface area due to different spatial atomic arrangements [23], metal ratios [24] or substances, e.g. Na^+ [25] or NO_3^- [14,26], showing an inhibiting effect during catalysis.

Therefore, a method to predict the phase composition of the aged precursor as a function of temperature, pH and reactant composition would be a desirable tool to adapt the preparation of Cu/Zn catalysts, e.g. to the changed syngas composition. Based on previous results [13], we propose that aging may be understood as a thermodynamic equilibrium process. Thus, a thermodynamic model should be able to predict the phase composition of the aged precursor.

Furthermore, these results coincide with studies showing that co-precipitation is completed in milliseconds to seconds [13,22,27]. In contrast, aging, in general, takes 30 min or several hours [10,28,29] before the phase transformation to zincian malachite is completed. According to recent studies by Güldenpfennig et al. at milliliter scale [30], this phase transformation seems to consist of a long induction period, which may be shortened by seeding, and a short transformation time. Seeding is a widespread tool in industrial crystallization processes to control processes in the metastable zone limit of primary nucleation and better control particle morphology and size distribution of the product. We aim to transfer the results by Güldenpfennig et al. to the liter scale and analyse the influence of seeding on the properties of the aged precursor and the precatalyst. Thus, the potential to optimize aging regarding the process time required and in terms of process control is to be evaluated.

2 Theoretical Basis

2.1 State of the art of precursor aging and its description

Cu/ZnO based catalysts show a high MeOH selectivity [31], stability [32] and activity [7,8,18] if the Cu and Zn atoms in the catalyst material are finely und homogeneously distributed on the nanoscale. Therefore, the goal of catalyst preparation is to produce such a material, e.g. by flame-spray pyrolysis [10,33,34] or by forming zincian malachite as the intermediate after aging in the aforementioned multi-step process [16]. If co-precipitation is conducted under high mixing intensities, a co-precipitate is formed which is already homogeneous on the nanoscale [13,17,23]. However, if aging is skipped, this material does not result in a good catalyst [17,23] emphasizing the role of aging in general and the importance of zincian malachite as an intermediate in particular.

The crystal lattice of zincian malachite is based on the mineral malachite ($Cu_2(OH)_2CO_3$). When malachite is formed from a solution containing Zn^{2+} or is in contact with such a solution, Zn^{2+} ions may substitute up to 27 mol% [35] or 31 mol% [36] of the Cu^{2+} ions, thus creating zincian malachite [37,38]. The naturally occurring variant with Zn fractions of approx. 42 mol% is called rosasite and shows small differences in the space group symmetry operators [38], but, according to Behrens et al., a discrimination between both forms is nearly impossible [35]. Additionally, Parádsasvárite, another mineral in the malachite-rosasite group with the chemical formula ($Zn_{1.91}Cu_{0.06}Mg_{0.02}$)($CO_3$)($OH$)$_2$ was discovered in 2008 [39-41]. However, it was not yet found in any synthetic material. Accordingly, only zincian malachite with a variable Zn fraction is considered in this study.

Studies showed the resulting catalyst improves its properties if the Zn fraction of zincian malachite is as close as possible to this maximum [36,37]. When Zn^{2+} ions are incorporated into the lattice, its parameters change accordingly. On basis of data by Behrens et al. [35] the following linear correlations (Eqs. (2) to (5)) can be found for the lattice parameters a_{zM}, b_{zM}, c_{zM} and β_{zM} as a function of the Zn fraction in zincian malachite as defined in Eq. (1), each

with a coefficient of determination of $R^2 > 0.99$. These four correlations can then be used in a Rietveld refinement to determine a mean Zn fraction in zincian malachite $\tilde{x}_{Zn,zM} \pm \sigma$ from the XRD diffractogram. Zwiener et al. determined similar correlations up to 31 mol% Zn [36]. However, these functions led to higher deviations in our evaluation than Eqs. (2) – (5). Furthermore, small amounts of aurichalcite were detected for the process parameters applied in Sect. 4.2 in samples with total Zn fractions of 30 – 35 mol%. Therefore, we exclusively used the data by Behrens et al. and assumed an upper boundary of $\tilde{x}_{Zn,zM} = 27$ mol%.

$$\tilde{x}_{Zn,zM} = \frac{n_{Zn^{2+},zM}}{n_{Zn^{2+},zM} + n_{Cu^{2+},zM}} \qquad (1)$$

$$a_{zM} \cdot Å^{-1} = -0.0045\ \tilde{x}_{Zn,zM} + 9.4938 \qquad (2)$$

$$b_{zM} \cdot Å^{-1} = 0.0056\ \tilde{x}_{Zn,zM} + 11.9131 \qquad (3)$$

$$c_{zM} \cdot Å^{-1} = -0.0024\ \tilde{x}_{Zn,zM} + 3.2451 \qquad (4)$$

$$\beta_{zM} \cdot (°)^{-1} = -0.0924\ \tilde{x}_{Zn,zM} + 98.7179 \qquad (5)$$

Experimental studies determined the process parameter ranges in which zincian malachite with $\tilde{x}_{Zn,zM}$ close to maximum forms predominantly. For Cu/ZnO/Al$_2$O$_3$ catalysts, the most widespread variant, 60 - 70 °C and pH = 6 - 7 should be chosen to obtain high amounts of zincian malachite [16]. In addition to pH and temperature, the ratio of Cu and Zn ions in the liquid phase is a dominant factor. If too few Zn^{2+} ions are available or not enough can be incorporated, the Zn fraction in zincian malachite is too low. If more than 27 % Zn^{2+} ions are present in the solids, by-product such as aurichalcite ($Zn_{(5-x)}Cu_x(OH)_6(CO_3)_2$) or hydrozincite ($Zn_5(OH)_6(CO_3)_2$) form. Although aurichalcite also consists of Cu and Zn, it results in a worse catalyst, probably due to too high Zn fractions of at least 60 mol% [37].

There are some studies using a kinetic crystallization model on the basis of population balance equations and thermodynamic data to describe und understand the co-precipitation step in the multi-step catalyst preparation [42-44]. However, there is no focus on aging. Yet, parts of the thermodynamic description and solubility data used can also be applied to aging.

Güldenpfennig et al. showed that the metal ratio, temperature and pH influence aging kinetics [30]. However, these parameters cannot be chosen freely since they also determine the physicochemical properties of the intermediate and thus catalyst properties. Therefore, they can only be varied to a limited extent. Guse et al. showed that the specific surface of the co-precipitate can almost be quadrupled by applying higher energy dissipation rates in the mixing of the two reactant solutions. Higher mass-specific surface areas appear to reduce improve aging kinetics significantly [13]. Yet, the most promising approach to improve aging kinetics respectively reduce aging times is apparently seeding. Güldenpfennig et al. could reduce the aging time by approx. 47 % by adding 4 % of the total solids mass as seeds: $x_{Seeds} = 0.04$, cp. Eq. (6) [30]. The higher the seed fraction, the shorter the indution time seemed to be. Currently, though, these results are limited to small volumes at the milliliter scale.

$$x_{Seeds} = \frac{m_{Seeds}}{m_{Solids,total}} \qquad (6)$$

Seeding is a standard procedure in many crystallization processes, e.g. to control the crystal morphology and the particle size distribution as they determine the filterability and flow properties of the particles in the downstream processes. They may also be crucial for the application, e.g. due to the resulting dissolution properties of proteins [45] or the surface and microstructure properties of the catalyst [13,20,21]. Seeding is likewise applied to improve control and the reproducibility of processes especially if small particles are involved or the

process is conducted in the range of the metastable zone limit of primary nucleation [46,47]. This way, it is also possible to enable secondary nucleation instead of uncontrolled primary nucleation and to control polymorphism [45,48-50]. In general, a minimum weight fraction of 0.1 – 1.0 w% is necessary to enable secondary nucleation below the metastable zone limit [51].

2.2 Thermodynamic modeling

The solubility product $K_{\mathrm{SP},j}$ according to Eq. (7) describes the equilibrium between the solids-forming ions i in the liquid phase and each solid phase j and is a function of the individual activities of each ion i of the solid j at thermodynamic equilibrium $a_{i,j}^*$ and its stoichiometric coefficient $\nu_{i,j}$.

$$K_{\mathrm{SP},j} = \prod {a_{i,j}^*}^{\nu_{i,j}} \qquad (7)$$

The driving force for solids formation during co-precipitation and aging is the phase-specific supersaturation S_j according to Eq. (8). It is described in terms of the actual activities of solids-forming ions a_i in the solution, the solubility product $K_{\mathrm{SP},j}(T)$ of the solid phase j and the stoichiometric coefficients ν_i and $\nu_{\pm}$. The activity a_i of an ion i can be calculated from its molality b_i, the reference value $b^0 = 1\ \mathrm{mol} \cdot \mathrm{kg}^{-1}$ and its activity coefficient γ_i according to Eq. (9). Thus, non-ideal ion interactions are considered.

$$S_j = \left(\frac{\prod a_{i,j}^{\nu_{i,j}}}{K_{\mathrm{SP},j}(T)} \right)^{1/\nu_{\pm}} \qquad (8)$$

$$a_i = \gamma_i \cdot \frac{b_i}{b^0} \qquad (9)$$

The amount of available solids-forming ions (free ions) is further reduced by speciation reactions or complex formation. The respective equilibrium is described with the ion association constant according to Eq. (10).

$$K_{\mathrm{IA},k} = \frac{a_k}{\prod a_{i,k}^{\nu_{i,k}}} \qquad (10)$$

Activity coefficient models for the calculation of γ_i vary in their number of ion- or ion-pair-specific parameters and accordingly in their range of validity. In general, activity coefficient models only consider ion interactions, but no ion associations. Hybrid models consider both. The reaction schemes for all solids forming ions (Cu^{2+}, Zn^{2+}, Zr^{4+}, Na^+, CO_3^-, NO_3^-) involve interactions with OH^- respectively H_3O^+ and, thus, influence the pH of the electrolyte [13]. Therefore, the pH of the electrolyte or aging suspension is an easily accessible measurand to observe the aging progress, but also to understand the underlying chemistry.

Four activity coefficient models are compared in Fig. 1a and 1b with regard to their applicability for Cu/Zn based catalyst precursors:
  I.   the Davies extended Debye–Hückel model (CHEAQS Next (64 bits, Version 0.2.1.3)) [42,52] without ion specific parameters ($I_{\mathrm{Davies}} \leq 0.5\ \mathrm{mol} \cdot (\mathrm{kg\,H_2O})^{-1}$)
  II.   the WATEQ model (WATEQ_minteq.v4) [53] with ion specific parameters ($I_{\mathrm{WATEQ}} \leq 1.0\ \mathrm{mol} \cdot (\mathrm{kg\,H_2O})^{-1}$)
  III. the Pitzer model with ion-pair specific parameters. Ion association reactions are only considered if the respective interaction parameters are unavailable ($I_{\mathrm{Pitzer}} \leq 6\ \mathrm{mol/l}$ [54]) [13]
  IV.   a modified hybrid Pitzer model where both Pitzer parameters and $K_{\mathrm{IA},k}$ are considered for the same ion pairing (cp. [13] but with re-activated ion association reactions)

First, pure reactant solutions without solid formation are considered in order to exclude a possible influence by solubility products.
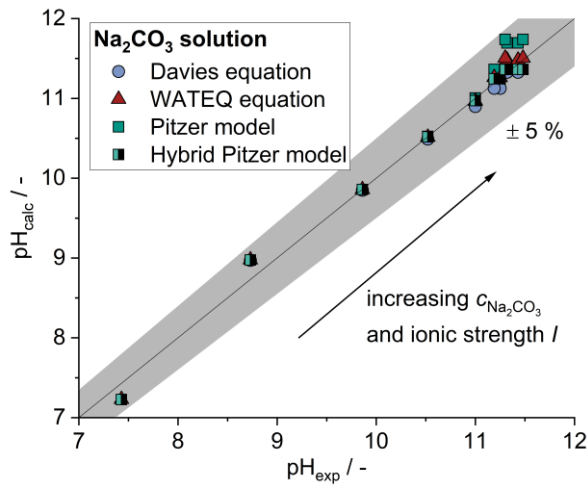
Figure 1a. Parity plots for calculated and experimentally determined pH for three different activity coefficient models for 8 different molalities of an aqueous Na_2CO_3 solution between $10^{-5}\ mol/kg\ H_2O < b_{Na_2CO_3} < 2\ mol/kg\ H_2O$ at 298 K.
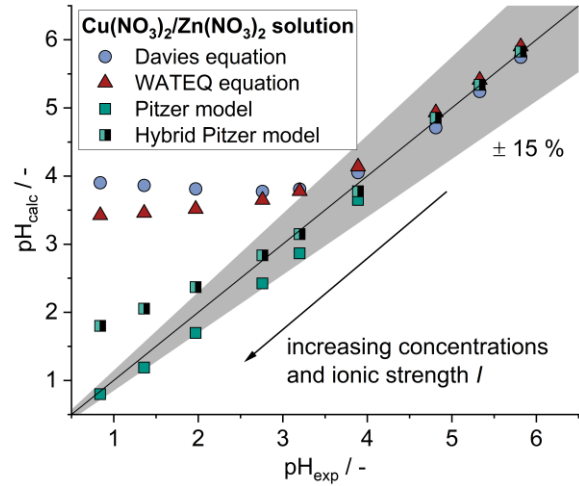
Figure 1b. Parity plots for calculated and experimentally determined pH for three different activity coefficient models for 9 different molalities of an aqueous $Cu(NO_3)_2/Zn(NO_3)_2$ solution at 298 K between $10^{-4}\ mol/kg\ H_2O < b_{metal\ nitrates} < 4\ mol/kg\ H_2O$. $n_{Cu(NO_3)_2}/n_{Zn(NO_3)_2} = 1$.

In Fig. 1a, the calculated pH of Na_2CO_3 solutions with varying molalities between 10^{-5} mol·(kg H_2O)$^{-1}$ and 2 mol·(kg H_2O)$^{-1}$ at 298 K is plotted against the measured pH. All four models show a good fit with deviations of less than 5 % across the entire range up to $I = 6\ \mathrm{mol} \cdot (\mathrm{kg\ H_2O})^{-1}$. Thus, all four models seem to correctly represent the complex formation and non-ideal interaction of Na^+ and $CO3^{2-}$ ions and accordingly calculate accurate activities for these species. A direct comparison of both Pitzer model variants shows that the hybrid approach is favorable for $I \geq 0.3\ \mathrm{mol} \cdot (\mathrm{kg\ H_2O})^{-1}$. In Fig. 1b, the same procedure is repeated for the other reactant solution, an aqueous mixture of $Cu(NO_3)_2$ and $Zn(NO_3)_2$ with $10^{-4}\ \mathrm{mol} \cdot (\mathrm{kg\ H_2O})^{-1} < m_{\mathrm{metal\ nitrates}} < 4\ \mathrm{mol} \cdot (\mathrm{kg\ H_2O})^{-1}$. Here, all models show deviations of less than 6 % when compared to the measured data for $pH_{\mathrm{exp}} > 3.9$, thus $I \leq 0.6\ \mathrm{mol} \cdot (\mathrm{kg\ H_2O})^{-1}$, which is in agreement with known ranges of validity. For higher molalities up to $I = 12\ \mathrm{mol} \cdot (\mathrm{kg\ H_2O})^{-1}$, the Davies and WATEQ models show deviations of 18 % to more than 300 %. The hybrid Pitzer model also shows deviations of more than 15 % for $I \geq 6\ \mathrm{mol} \cdot (\mathrm{kg\ H_2O})^{-1}$. In contrast, deviations for the Pitzer model remain below 15 %. Yet, in the range of $0.6\ \mathrm{mol} \cdot (\mathrm{kg\ H_2O})^{-1} < I < 3\ \mathrm{mol} \cdot (\mathrm{kg\ H_2O})^{-1}$ ($2.8 < pH < 3.9$), the hybrid variant is more accurate which has been predicted by Pitzer et al. by talking about "maxima of association" in certain concentration ranges depending on the stoichiometry of ion pairings [55].

Even relatively simple activity coefficient models like the Davies approach are suited to describe Na^+ and $CO3^{2-}$ based electrolytes. However, for the more complex behavior of $Cu(NO_3)_2$ and $Zn(NO_3)_2$ solutions, a more sophisticated approach becomes necessary, e.g. the use of a Pitzer model variant. Since the reactant solutions show an opposite trend comparing both Pitzer approaches, ion association reactions have to be considered only if proven necessary as suggested in general by Lassin et al. [56]. Thus, the applicability of solubility products of minerals for the thermodynamic description of aging will be discussed separately in Sect. 4.1 using a Pitzer model modified accordingly.

3 Materials and Methods

3.1 Materials and Model

A ternary Cu/Zn/Zr based catalyst precursor produced according to Sect. 3.2 is used in this study to evaluate the predictability of the phase composition in the aged precursor using a thermodynamic model and to characterize the influence of seeding on both aging kinetics and properties of the aged precursor. The reactant solutions were prepared from $Cu(NO_3)_2 \cdot 3H_2O$ (purity ≥ 99.5 %, Merck), $Zn(NO_3)_2 \cdot 6H_2O$ (purity ≥ 99 %, Alfa Aesar), $ZrO(NO_3)_2 \cdot 6H_2O$ (purity > 99 %, Sigma-Aldrich), $NaHCO_3$ (purity ≥99 %, Carl Roth) and demineralized water. In some studies a HNO_3 solution (65%, Carl Roth) and NaOH (purity ≥99 %, Carl Roth)) were used to adjust the initial pH after co-precipitation. For the study on the influence of the metal ratio discussed in Fig. 3 Na_2CO_3 (purity ≥99 %, Carl Roth) and a binary Cu/Zn based catalyst precursor were used instead.

We consider four kinds of intermediates: 1) the co-precipitate directly after co-precipitation is completed ($t_{age} = 0$ min), 2) samples taken at defined moments (t_{age}) during aging, 3) the aged precursor after aging is completed and 4) the precatalyst consisting of CuO, ZnO and ZrO_2 and obtained by calcination.

The software PHREEQC (iphreeqc Version 3.7.1) is used to calculate the thermodynamic state of equilibrium for aging. A modified database on the basis of PITZER.DAT [13] containing information on the activity coefficient model as well as literature data for $K_{IA,k}$ and $K_{SP,j}$ is applied. The following solids were relevant at the considered parameter ranges: rosasite (zincian malachite) [44], malachite [57], aurichalcite [58], hydrozincite [59] and ZrO_2 [60]. PHREEQC solves mass and substance balance equations and calculates speciation of ions in the liquid phase. By iteration, these calculations are repeated until all phases considered are saturated or undersaturated. An ideally mixed and isotherm system as well as no interaction with any gas phase are assumed. Any CO_2 formed is dissolved in the liquid phase as a separate species so that no interaction with the ambient air is considered.

3.2 Experimental Set-up and Procedure

Based on results on the influence of mixing in co-precipitation [13], continuous co-precipitation and batch aging were strictly separated according to Fig. 2. A $NaHCO_3$ solution (feed 1) and a metal nitrate solution (feed 2) with equal volume flows were continuously mixed by an impinging micro jet mixer. Co-precipitation then takes place. The dimensions of the mixer are given in Fig. 2 in mm. Two gear pumps (MCP-Z Standard, Ismatec with GJ-N23 pump heads, Micropump) in combination with magnetic-inductive flow meters (IFC90, Krohne) were used at constant total volume flows of 600 ± 40 mL·min^{-1}. Deviations results from the collision of the two reactant streams and the associated highly sensitive control system. Regarding all experiments at $pH(t_{age} = 0 \text{ min}) = 7.1$, $T = 55\,°C$, $b_{NaHCO_3,Feed1} = 1.018 \text{ mol} \cdot (\text{kg H}_2\text{O})^{-1}$, $b_{Cu(NO_3)_2,Feed2} = 0.162 \text{ mol} \cdot (\text{kg H}_2\text{O})^{-1}$, $b_{Zn(NO_3)_2,Feed2} = 0.081 \text{ mol} \cdot (\text{kg H}_2\text{O})^{-1}$ and $b_{ZrO(NO_3)_2,Feed2} = 0.027 \text{ mol} \cdot (\text{kg H}_2\text{O})^{-1}$ were used. The temperature of co-precipitation and aging was adjusted for the temperature study in Fig. 4. The experiments with $pH(t_{age} = 0 \text{ min}) = 6.7$ were conducted using the same molalities but by additionally adding a 65% HNO3 solution to feed 2: $X_{HNO_3,Feed2} = 22 \text{ mL} \cdot (\text{kg H}_2\text{O})^{-1}$. The pH for the pH study in Fig. 5 was adjusted by additionally adding HNO_3 or NaOH to the reactant solutions while maintaining constant concentrations of $NaHCO_3$ and the metal reactants. For the binary Cu/Zn based precursor discussed in Fig. 3 $b_{Na_2CO_3,Feed1} = 0.6 \text{ mol} \cdot (\text{kg H}_2\text{O})^{-1}$, $b_{Cu(NO_3)_2,Feed2} + b_{Zn(NO_3)_2,Feed2} = 0.5 \text{ mol} \cdot (\text{kg H}_2\text{O})^{-1}$ and $T = 65\,°C$, were applied.

The co-precipitate suspension was fed directly into one of two double-jacketed 4000 mL glass tank reactor ($d_{tank} = 120 \text{ mm}$) with four baffles according to DIN 28131, where aging took place under stirring with a two-staged three-blade propeller agitator ($d_{stirrer,1} =$

40 mm; $d_{\text{stirrer,2}} = 50\,\text{mm}$, 30° pitch) at 1000 rpm. The pH was measured with a HI1190T electrode (Hanna). The pH electrode was calibrated daily with two reference solutions (HI 70004 and HI 70007 for $4 < pH < 7$ or HI 70007 & HI 70010 for $7 < pH < 10$, respectively by Hanna). Temperature was controlled with ±1 K accuracy. Samples during aging were obtained by withdrawing 30 mL – 50 mL suspension near the stirrer. These samples were processed identically to the co-precipitate suspension, as described in Sect. 3.3. In general, aging was completed 30 min after a pH minimum has occurred.
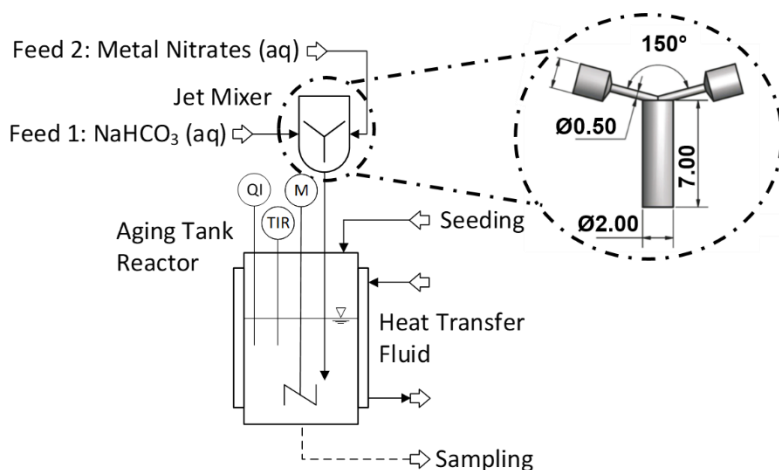
Figure 2. Experimental setup for a continuous co-precipitation followed by batch aging. M: motor, TCR: temperature control and recording, QR: pH recording. Based on [13].

The suspension of both the time samples and the aged precursor was collected without dilution for the analytics described in Sect. 3.3. It was then filtered (MN85/70, Macherey-Nagel or similar) using a water aspirator. The filter cake was suspended and washed with demineralized water until an electrical conductivity of < 50 µS·cm-1 was achieved and no nitrate could be detected by nitrate test strips (< 10 mg·L-1, VWR Chemicals). The moist sample was then dried at the aging temperature for at least 15 h. Some samples were then calcined as described elsewhere [10] and ground in a mortar until no more lumps can be visually detected.

Dried seeding material was obtained by completing an aging at the same process conditions as the intended seeding experiment and then washing, drying and grinding the solids as described above. Seeding suspensions were obtained by conducting aging until the pH minimum is reached and then withdrawing the desired amount of suspension. For certain studies the seeding suspension was concentrated by filtration and resuspension of the filter cake in a suspension with the original solids content. Dried seeding material and seeding suspensions were added by syringe or funnel from the top of the reactor directly after co-precipitation was finished. Seeding was completed within a maximum of 2 min. Inverse seeding was realized by aging a small volume until aging is completed and then adding fresh co-precipitate suspension to the aged suspension.

3.3   Analytics

Fourier-transform infrared spectroscopy (FT-IR) and X-ray diffraction (XRD) measurements of the dried and ground samples were used to determine the phase composition of the solids. The FT-IR spectra in the range of 4000 cm-1 $< \tilde{v} <$ 230 cm^{-1} with a resolution of 2 cm^{-1} were measured using a Varian 660-IR spectrometer (Agilent) in combination with the software Resolution Pro and the KBr disc technique [29]. X-ray diractograms in the range of 5° $< 2\theta <$ 80° were measured using a Panalytical X'Pert Pro X-ray diffractometer (Malvern Panalytical) with Bragg-Brentano geometry and Cu K-α radiation with a Ni filter over a period of 120 min. Some samples were measured with a STOE STADI MP instead. A Rietveld refinement was used to determine mass fractions of solids phases from the diffractogram. For this purpose the software Profex Version 4.3.5 was used [61]. The following reference data were used:

malachite (BGMN [61]), modified according to Eqs. (2) – (5), hydrozincite (BGMN), aurichalcite (RRUFF ID R060426.1), $Na_2Zn_3(CO_3)_4 \cdot 3H_2O$ (ICSD 81305), ZrO_2 (ICSD 83862 and 18190), β-$Zr(OH)_2(NO_3)_2 \cdot 5(H_2O)$ (ICSD 84658), $Zr(OH)_3NO_3$ (ICSD 80062), CuO (04-007-1375, Ceramics, Profex) and Zincite (BGMN).

XRF measurements to determine metal ratios of the samples were conducted using a Bruker Pioneer S4 [10]. Elemental analysis was performed with a vario EL cube (Elementar). A 725 ICP-OES spectrometer (Agilent) was used for complementary ICP-OES measurements. Solid samples for ICP-OES measurements were digested beforehand using a Multiwave 3000 (Anton Paar) with an added acid for 2 h at a maximum of 60 bar and 240 °C. The specific particle surface areas (S_{BET}) of the precatalysts were determined by N_2 physisorption measurements using a Quantachrome NOVA 2000e device (Anton Paar) at 77 K. Samples were degassed for 12 h at 120 °C. Isotherms were evaluated with the Brunnauer-Emmett-Teller model (BET) in the range of $0.01 - 0.5$ p/p_0. The particle morphology was analyzed by scanning electron microscopy (SEM) with a Zeiss GeminiSEM 500 with a Schottky field emission cathode. The particles of the dried sample were fixated on adhesive carbon pads. In order to complement the metal composition determined by ICP-OES and XRF measurement, additional EDXS measurements using an Oxford X-Max[N] system were conducted.

4   Results and Discussion

As discussed in Sect. 1 and 2.1 aging is crucial for the aforementioned product qualities of the final catalyst. The studies here aim to help improving the aging process on two levels. First, in Sect. 4.1 phase compositions calculated with a thermodynamic model are compared to experimental data to resolve if the phase composition after aging can be predicted. Then, in Sect. 4.2 the influence of seeding with different techniques and mass fractions will be discussed to quantify how far seeding can accelerate the aging process at liter scale.

4.1   Model Based Prediction of the Phase Composition

Three main factors that significantly influence the aged intermediate have been established in the experimental studies discussed previously: the Cu/Zn ratio, pH and temperature [7,16]. Therefore, the applicability of the thermodynamic model to predict phase composition after aging shall be discussed on basis of these parameters.

In Fig. 3a the mass fractions of the solids phases of the aged intermediate are plotted as a function of the total Zn fraction $\tilde{x}_{\mathrm{Zn,Feed2}}$ in the metal reactant solution as defined in Eq. (11) for a simplified binary Cu/Zn based catalyst precursor. The mass fractions of the experimental samples (dots) were determined by XRD and a Rietveld refinement as described in Sect. 3.3. Therefore, only crystalline portions of the solid can be registered. Process conditions corresponding to the experimental conditions were applied for the calculated data (lines). In Fig. 3b the corresponding molar fraction of Zn in zincian malachite $\tilde{x}_{\mathrm{Zn,zM}}$ is plotted as a function of $\tilde{x}_{\mathrm{Zn,Feed2}}$.

$$\tilde{x}_{\mathrm{Zn,Feed2}} = \frac{b_{\mathrm{Zn,Feed2}}}{b_{\mathrm{Cu,Feed2}} + b_{\mathrm{Zn,Feed2}}} = \frac{b_{\mathrm{Zn(NO_3)_2,Feed2}}}{b_{\mathrm{Cu(NO_3)_2,,Feed2}} + b_{\mathrm{Zn(NO_3)_2,,Feed2}}} \qquad (11)$$

For $\tilde{x}_{\mathrm{Zn,Feed2}} = 0$ mol%, Cu is present as the only metallic reactant. Accordingly, only pure malachite (equal to zincian malachite with $\tilde{x}_{\mathrm{Zn,zM}} = 0$) is formed as shown by the thermodynamic model and confirmed experimentally in Fig. 3a and 3b. Only zincian malachite continues to be formed for increasing Zn fractions in the feed of up to $\tilde{x}_{\mathrm{Zn,Feed2}} = 20$ mol%. Concurrently, the Zn fraction in zincian malachite increases in both the model and the experiments. While the model shows zincian malachite as the only product up to $\tilde{x}_{\mathrm{Zn,Feed2}} = 30$ mol%, the Rietveld refinement indicates, contrary to expectations, small amounts of aurichalcite. For higher $\tilde{x}_{\mathrm{Zn,Feed2}}$, aurichalcite is increasingly formed as an additional phase. The XRD evaluation also shows the existence of hydrozincite which is only present in the model above $\tilde{x}_{\mathrm{Zn,Feed2}} = 50$ mol%. For $\tilde{x}_{\mathrm{Zn,Feed2}} = 1$ aurichalcite with $\tilde{x}_{\mathrm{Cu,Aur}} = 0$ is formed

exclusively both in the model and experimentally. Discrepancies between predicted fractions and the values determined by Rietveld refinement can be seen in particular for $0.3 < \tilde{x}_{Zn,Feed2} < 0.6$ when the predominance swaps between zincian malachite and aurichalcite. Probable reasons for these deviations are on the one hand the scarcity of thermodynamic data for the synthetic phases. For this reason, $K_{SP,j}$ of mineral phases with fixed stoichiometries deviating from the experimentally determined metal ratios in the solids had to be used. The difference in the maximum of $\tilde{x}_{Zn,zM}$ between model and XRD evaluation can also be explained with differences in the maximum Zn fraction of zincian malachite between the thermodynamic data used in the model and the boundaries applied in the Rietveld refinement. On the other hand, the use of the two distinct mineral phases aurichalcite and hydrozincite with fixed Zn and Cu fractions and thus relatively fixated lattice parameters may also result in uncertainties in the Rietveld refinement. Yet, the general trends for the phase composition after aging and the Zn fraction in zincian malachite are predicted correctly by the thermodynamic model.
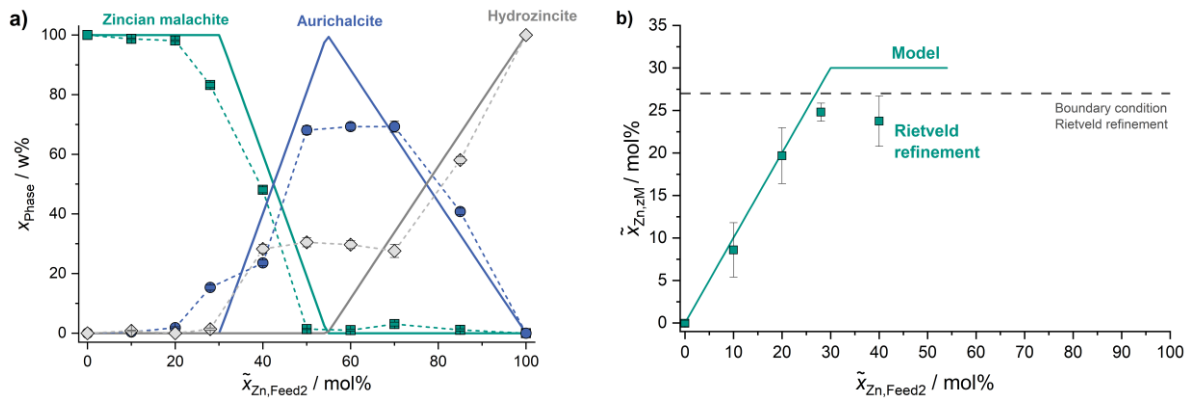
Figure 3. Mass fraction of solids phases in the aged intermediate (a) and the zinc fraction in zincian malachite $\tilde{x}_{Zn,zM}$ (b) as a function of the Zn fraction in the metal reactant solution $\tilde{x}_{Zn,Feed2}$ at 65 °C.

In Fig. 4a the mass fractions of the solids phases after aging are plotted as a function of temperature for $\tilde{x}_{Zn,Feed2} = 0.33$. In Fig. 4b $\tilde{x}_{Zn,zM}$ is plotted accordingly.
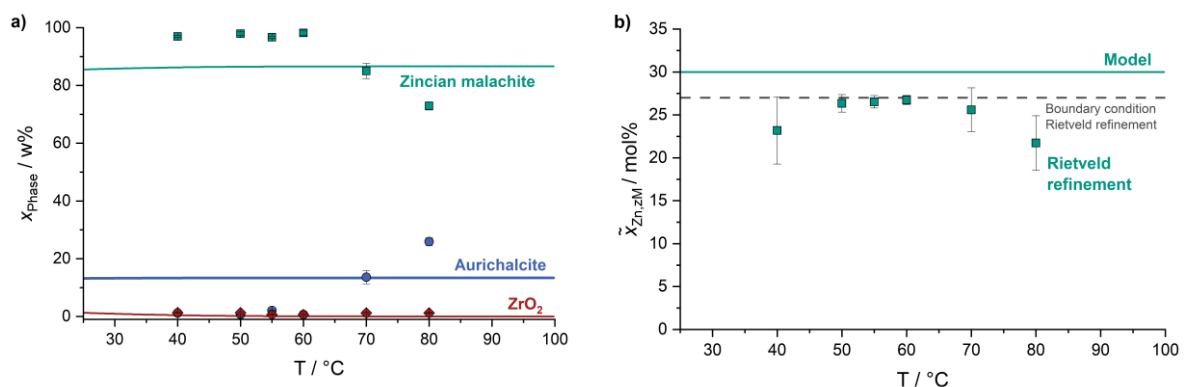
Figure 4. Mass fraction of solids phases in the aged intermediate (a) and the zinc fraction in zincian malachite $\tilde{x}_{Zn,zM}$ (b) as a function of temperature for $\tilde{x}_{Zn,Feed2} = 0.33$.

Both model and experiments show a predominance of zincian malachite for $T \leq 60\ °C$ with a ratio of approx. 9 to 1. Deviations can be explained with differences in the Cu and Zn fractions between the literature data used in the thermodynamic model and the Rietveld refinement for both zincian malachite (30 vs. 27 mol% Zn) and aurichalcite (45.4 vs. 37.5 mol% Cu). These differences also explain the deviations in the determined $\tilde{x}_{Zn,zM}$. For higher temperatures, the experiments show an increasing fraction of aurichalcite of up to 26 mol% and decreasing Zn fractions in zincian malachite. Since no temperature-dependent $K_{SP,j}$ are available, the model does not show any temperature dependency. Using reaction enthalpies calculated from standard formation enthalpies and the simplified van't Hoff equation according to Eq. (12) with

the reaction enthalpy at T_0 $\Delta_r H^0$ and the gas constant R instead to depict temperature effects does not show significant differences. Therefore, only the latter variant is shown.

$$K_{\mathrm{SP},j}(T) = K_{\mathrm{SP},j}(T_0) \cdot \exp(-\frac{\Delta_r H^0}{R\,T} + \frac{\Delta_r H^0}{R\,T_0}) \qquad (12)$$

In Fig. 5a, the experimentally determined mass fractions of the solids phases of the aged precursor are plotted as a function of the initial pH directly after co-precipitation took place ($t_{\mathrm{Age}} = 0$ min) for $\tilde{x}_{\mathrm{Zn,Feed2}} = 0.33$. The model data shows the phase fractions as a function of the pH at thermodynamic equilibrium. In Fig. 5b $\tilde{x}_{\mathrm{Zn,zM}}$ is plotted accordingly.
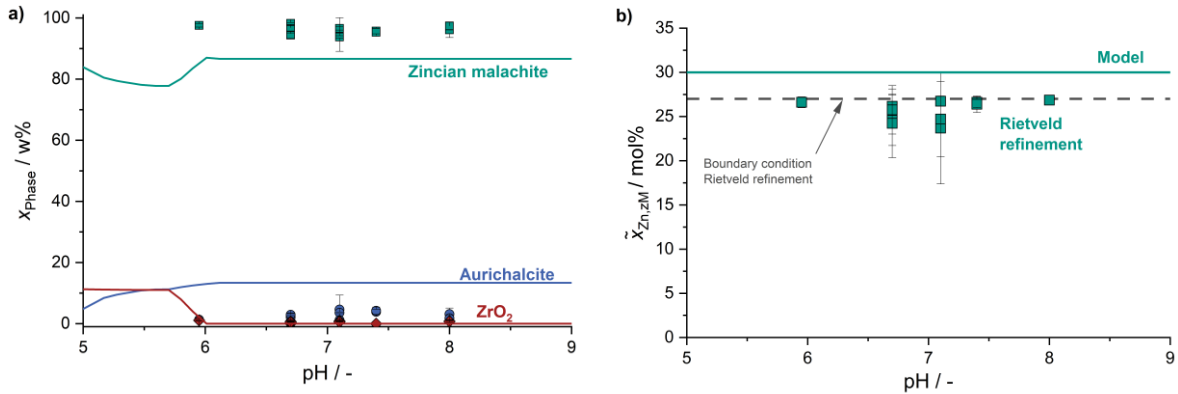
Figure 5. Mass fraction of solids phases in the aged intermediate (a) and the zinc fraction in zincian malachite $\tilde{x}_{\mathrm{Zn,zM}}$ (b) as a function of pH for $\tilde{x}_{\mathrm{Zn,Feed2}} = 0.33$.

The Rietveld refinement reveals the same phase composition for each sample independent from the initial pH. The model shows the same trend, but lower mass fractions for zincian malachite. Similar deviations also result for $\tilde{x}_{\mathrm{Zn,zM}}$ in Fig. 5b. Again, this can be explained with differences in the stoichiometries of zincian malachite and aurichalcite between the thermodynamic model and the reference data used in the Rietveld refinement.

In general, the thermodynamic model was able to predict the predominance of zincian malachite after aging for the pH and temperature ranges investigated. For varying reactant compositions, the model was able to correctly determine the change between an aged precursor rich in zincian malachite and rich in aurichalcite and the increasing Zn fraction in zincian malachite. Quantitative deviations for the phase composition and $\tilde{x}_{\mathrm{Zn,zM}}$ between the model and the results of the Rietveld refinement can be explained with inconsistent molecular formula for the solid phases considered and missing thermodynamic data for synthetic phases.

4.2 Accelerating Aging by Seeding

Aging takes much longer than co-precipitation, presumably mainly due to the induction time described by Güldenpfennig et al. [30]. A method to reduce this induction period while maintaining the properties of the aged intermediate and thus those of the final catalyst material would help to optimize aging economically and to better control the process. First, it will be discussed if seeding does have a significant impact on aging kinetics at liter scale and how this influence may be increased by varying the seed mass fraction or the seeding method. Then, the influence of seeding on the phase and metallic composition as well as the surface properties of the aged precursor and the precatalyst, known to correlate with the quality of the final catalyst, will be quantified. Finally, the transferability to other process conditions will be analysed and the significance of seeding will be assessed on this basis.

In Fig. 6a, the pH profile is plotted as a function of the aging time for seven independent experiments. The general progression over time will be discussed exemplarily using one curve (red line). The other curves are intended to show the reproducibility. In Fig. 6b, the same aging conditions were applied but seeds were added directly after co-precipitation is completed.
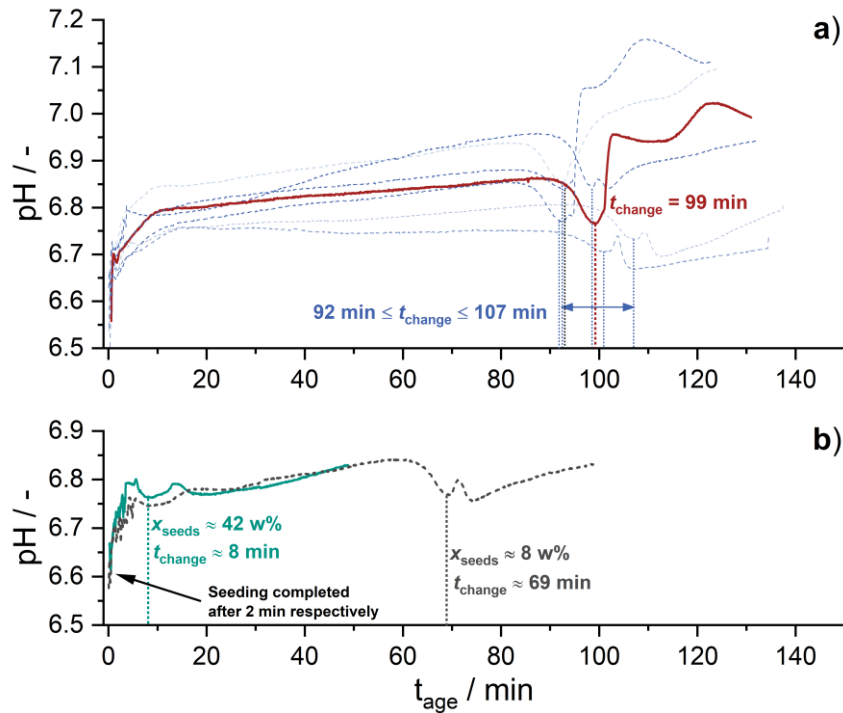
Figure 6. pH profiles as a function of aging time for (a) seven independent unseeded experiments with one progress marked exemplary for discussion and (b) two seeded experiments with different seed weight fractions.

The curves in Fig. 6a all show a similar trend. First, during wetting of the pH electrode, the pH rises rapidly up to the intended start value of $pH(t_{age} = 0 \text{ min}) = 6.7$. It then quickly continues to rise to $pH \approx 6.75 - 6.8$ in the first approx. 10 min from where the pH is almost stable or rises only slightly. After a total aging time of 92 to 107 min a pH minimum is passed which coincides with a change in color, s. Fig. 7, and indicates that the phase change to zincian malachite happens [16,28,62].

Figure 7. Color change during aging: the reactors in the background and on the left respectively show a blue color before the phase change begins ($t_{age} \ll t_{change}$). The reactors in the front and on the right respectively are greenish after zincian malachite was formed ($t_{age} \gg t_{change}$).

Furthermore, the formation of zincian malachite results in a change in crystallinity which will be discussed in Fig. 9ff. To ensure that the phase change is completed, aging is continued for additional 30 min. In some cases, a second pH minimum could be observed but not correlated to any events or altered properties. The three stages of rapid pH increase, slow increase and pH minimum can also be identified in both seeded experiments in Fig. 6b. However, depending

on the seed mass fraction chosen, the minimum already occurs at 69 min for $x_{\text{Seeds}} = 8$ w% or after just 8 min for $x_{\text{Seeds}} = 42$ w%. Thus, an influence of x_{Seeds} on the necessary aging time is present and will be quantified.

In Fig. 8 the turnover point indicating the phase change to zincian malachite is shown as a function of the seeding mass fraction x_{Seeds}. Both the quantitative method following the pH minimum and a simple optical method based on a change in color are shown. Each point is an individual experiment.
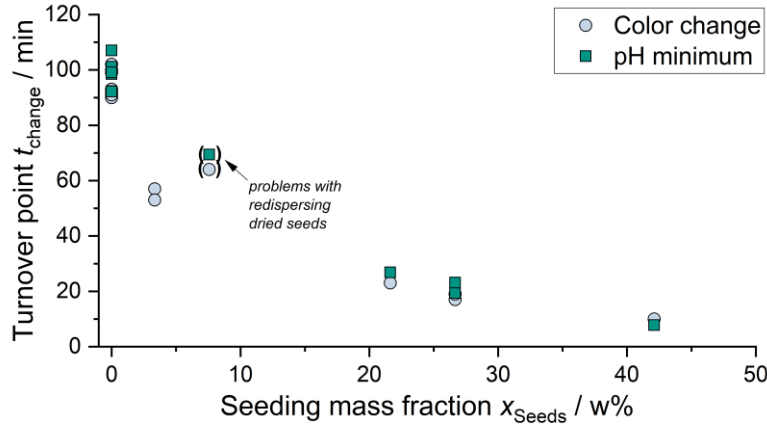
Figure 8. Time of the phase change as a function of seeding mass fraction. Both the quantitative method following the pH minimum and a simple optical method based on a change in color are shown.

Without seeding the phase change occurs after an average of $\bar{t}_{\text{change}} = 96 \pm 5$ min and a minimum of $t_{\text{change,min}} = 90$ min. The higher the seeding mass fraction, the faster the turnover point is reached. Already for $x_{\text{Seeds}} = 3$ w%, the necessary time is reduced by 43 % to only $\bar{t}_{\text{change}} = 55 \pm 3$ min. Higher x_{Seeds} lead to increasingly short turnover times resulting in $t_{\text{change}} = 8$ min for the highest seeding mass fraction considered. Güldenpfennig et al. found a similar trend at milliliter scale by varying x_{Seeds} between 4 % and 20 % [30]. A runaway is observed for $x_{\text{Seeds}} = 8$ w% where dried seeding material was used instead of a suspension with freshly aged seeds. The unexpected late turnover point is probably due to the poor wettability and aggregation of the dry particles reducing the mass-specific surface area. For $x_{\text{Seeds}} = 27$ w% inverse seeding as described in Sect. 3.2 was additionally tested (points not specially marked), but no significant differences to the standard method are evident. The total yield of dried aged intermediate $Y_{\text{aged precursor,total}}$ is defined according to Eq. (13) and increases with increasing x_{Seeds} from 11.2 ± 1.4 g·L^{-1} for the unseeded experiments to 19.0 g·L^{-1} for $x_{\text{Seeds}} = 42$ w%. The yield of new solid $\Delta Y_{\text{aged precursor}}$ where the added seeding mass is substracted is defined by Eq. (14) with $\Delta Y_{\text{aged precursor}} = Y_{\text{aged precursor,total}}$ for unseeded experiments. A mean value of $\Delta \bar{Y}_{\text{aged precursor,seeded}} = 11.6 \pm 1.2$ g·L^{-1} for all seeded experiments indicate that seeding does not influence the yield as expected for a reaction which is dominated by the thermodynamic equilibrium. A higher mass fraction of seeds leads to a larger specific surface area of the solids during aging when assuming constant particle size distributions. According to Zander et al. the phase transformation occurs via the liquid phase [63]. Thus, the larger surface area when more seeds are present may explain the increasingly rapid transformation.

$$Y_{\text{aged precursor,total}} = \frac{m_{\text{dried aged precursor,total}}}{V_{\text{Suspension,total}}} \qquad (13)$$

$$\Delta Y_{\text{aged precursor}} = \frac{m_{\text{dried aged precursor,total}} - m_{\text{Seeds}}}{V_{\text{Suspension,total}}} \qquad (14)$$

The aging process was also observed by means of XRD samples taken every 20 min. A Rietveld refinement with the references and parameters listed in Sect. 3.3 and 2.1 was used to evaluate the solids phase composition. In Fig. 9 the general procedure is shown for an aged precursor and a precatalyst both prepared with $x_{\text{Seeds}} = 0$ w%.
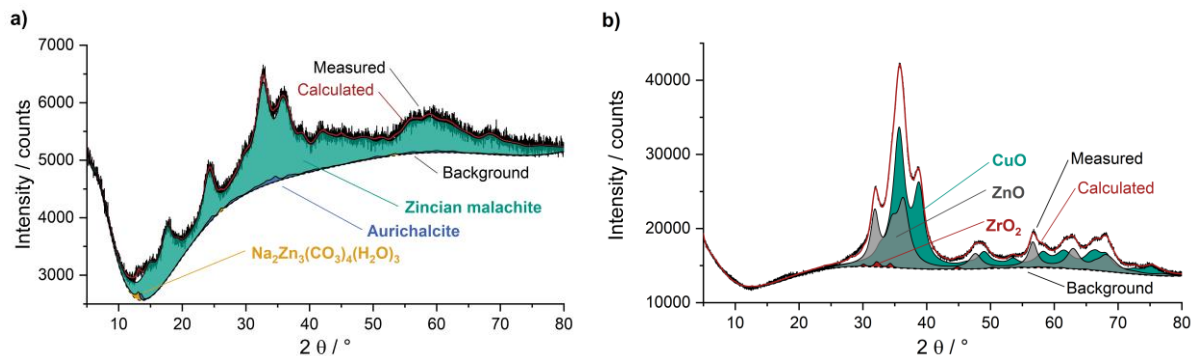
Figure 9. Exemplary Rietveld refinement of an aged precursor and a precatalyst (respectively: $x_{\text{Seeds}} = 0$ w%).

This procedure is then used in Fig. 10 a) to d) to observe the solids phase composition evolution during aging for x_{Seeds} between 0 w% and 42 w%. The range of turnover points determined by color change and pH minimum is marked as a hatched area. In Fig. 10 e) to h) the respective corresponding molar Zn fraction in zincian malachite $\tilde{x}_{\text{Zn,zM}}$ determined according to Sect. 2.1 is plotted. For $x_{\text{Seeds}} = 0$ w% the total Zn fraction in the solids was additionally quantified by means of ICP-OES and XRF.

For $x_{\text{Seeds}} = 0$ w% (Fig. 10a) the first three samples show an amorphous diffractogram. At the same time, the XRF measurements in Fig. 10e indicate a constant Zn fraction in the solids over the entire aging process with only small fluctuations without a visible trend. This implies the existence of one common amorphous Cu/Zn predecessor phase (zincian georgeite) or multiple amorphous phases in the initial stage of aging what is consistent with the literature [15,63,64]. The first crystalline structures are present in the 80 min sample. However, the evaluation of $\tilde{x}_{\text{Zn,zM}}$ shows high uncertainties up to 100 min indicating a change in crystal structure is taking place. Only after the phase change, as indicated by the pH minimum and color change, is completed, consistently high Zn fractions in the expected range of $\tilde{x}_{\text{Zn,zM}} \approx 0.27$ prevail. In general, the total Zn fractions determined with ICP-OES and XRF are in the range of 0.277 to 0.321 and thus slightly higher than expected. A possible explanation is the existence of small amounts of Zn rich aurichalcite or hydrozincite which was confirmed by the Rietveld refinement: 0.3 w% $< x_{\text{Aur,End}} < 2.6$ w%.

If seeds are added, a crystalline structure can be detected accordingly in the first time sample. For low x_{Seeds} only a small amount of crystalline material is present in the sample, thus only weakly pronounced peaks exist and result in high deviations. As well as for the unseeded experiments, some deviations for x_{zM} from $x_{\text{zM}} > 95$ % (Fig. 10b to d) and for $\tilde{x}_{\text{Zn,zM}}$ from $\tilde{x}_{\text{Zn,zM}} \approx 0.27$ (Fig. 10f to h) exist for $x_{\text{Seeds}} > 0$ w% for aging times below the turnover points determined by pH minimum and color change. After the apparent phase change is completed, $x_{\text{zM}} > 95$ % and $\tilde{x}_{\text{Zn,zM}} \approx 0.27$ result for all seeded experiments. This confirms the acceleration of aging by seeding also at the scale of the crystal lattice.
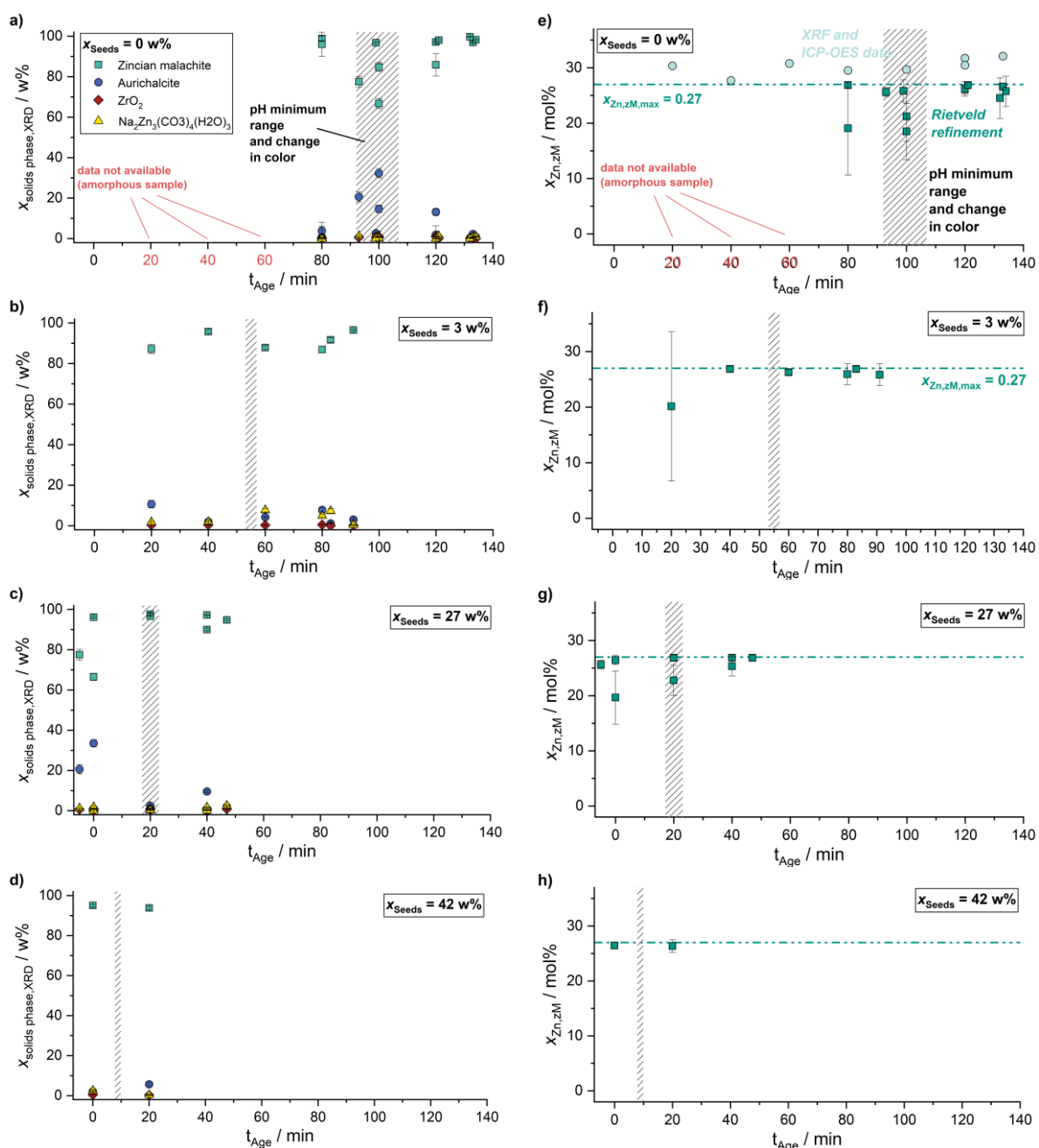
Figure 10. Solids phase composition as a function of aging time for four different seeding mass fractions (a to d) and Zn fraction in the zincian malachite phase determined by Rietveld refinement (e to h).

Fig. 11a shows the final solids phase composition of the aged precursor as a function of x_{Seeds}. For all x_{Seeds} except two outliers the fraction of zincian malachite is between 92 % and 100 %. No significant correlation between x_{zM} and x_{Seeds} is evident. Thus, the thermodynamic model discussed in Sect. 4.1 can be used for both seeded and unseeded aging. In Fig. 11b, the solids phase composition of the resulting precatalysts is plotted as a function of x_{Seeds}. The mass fractions of CuO x_{CuO} are between 48 % and 65 %, 33 % $< x_{\text{ZnO}} <$ 46 % and 1 % $< x_{\text{ZrO}_2} <$ 7 % if the data for $x_{\text{Seeds}} = 8\,\text{w\%}$, the only set showing high deviations, is excluded. The measured metal fractions discussed in Table 1 indicate much more consistent results in between experiments. Thus, the deviations in Fig. 11b are attributed to differences in crystallinity as well as inaccuracies in the Rietveld refinement where in some cases the relative error between measured and calculated curve were in the range of $2 < X^2 < 3$ and thus above the target value of $X^2 = 1.5$. Within the scope of these inaccuracies no correlation between the

solids phase composition of the precatalyst and the mass fraction of seeding material is evident. More fixated boundary conditions, e.g. a fixed metal composition based on ICP-OES or XRF analysis of the sample, should improve the accuracy of the Rietveld refinement in the future.
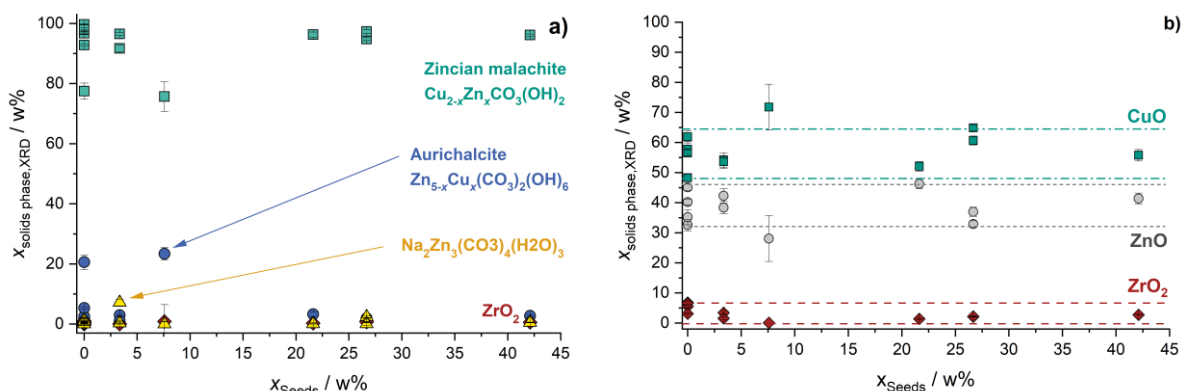
Figure 11. Solids phase composition of (a) the aged precursor and (b) the precatalyst as a function of the seeding mass fraction.

In Fig. 12 excerpts of complementary FT-IR measurements for respectively two experiments for $x_{\text{Seeds}} = 0\,\text{w}\%$ and $x_{\text{Seeds}} = 3\,\text{w}\%$ are shown. The spectra for both operating modes are congruent except for the two marked areas. The peak in the area 1163 cm^{-1} is most similar to the reference spectrum for rosasite analyzed by Stoilova et al. [65]. According to the authors, a peak in the range 960 – 971 cm^{-1} can be attributed to hydrozincite or aurichalcite. This may indicate a low level of aurichalcite or hydrozincite accumulation in the use of seeding. However, the XRD data shown in Fig. 11 show no significant influence. Therefore, future studies should characterize the impact of repeated use of the same seeding material on the hydrozincite and aurichalcite fractions in the aged precursor.
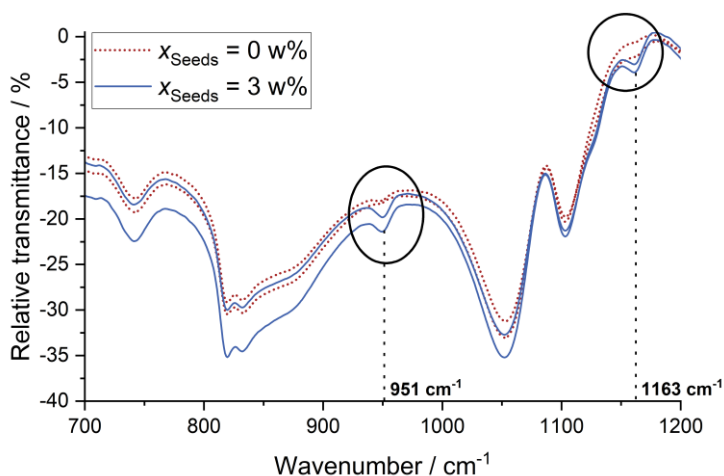
Figure 12. FTIR spectra of, respectively, two aged precursors prepared by unseeded ($x_{\text{Seeds}} = 0\,\text{w}\%$) and seeded aging ($x_{\text{Seeds}} = 3\,\text{w}\%$). Complete measuring range: $0 - 4000\,\text{cm}^{-1}$.

Fig. 13 shows SEM images of two aged precursors from an unseeded (left) and seeded ($x_{\text{Seeds}} = 3\,\text{w}\%$, right) aging at two different magnifications. Both the overview image and the detail shot show a very similar morphology in either case. This implies that the reduced aging time resulting from seeding does not influence the morphology and in particular the microstructure. Table 1 provides an overview on how seeding may influence properties of the resulting precatalyst. Additionally to the experiments at $pH(0\,\text{min}) = 6.7$, data for $pH(0\,\text{min}) = 7.1$ is specified. For $pH(0\,\text{min}) = 7.1$ aging could also be accelerated by approx. 50 % reducing the necessary aging time from an average of 76 min to 38 min by adding a seeding mass fraction of $x_{\text{Seeds}} = 3\,\text{w}\%$.
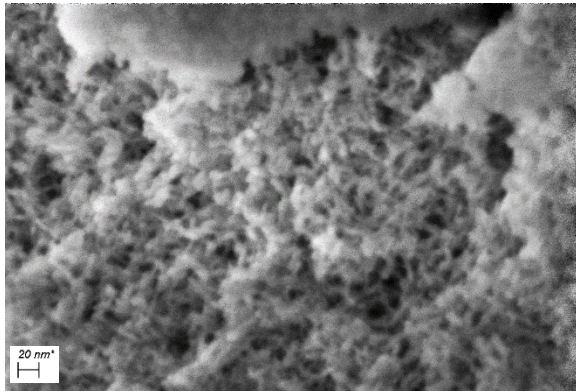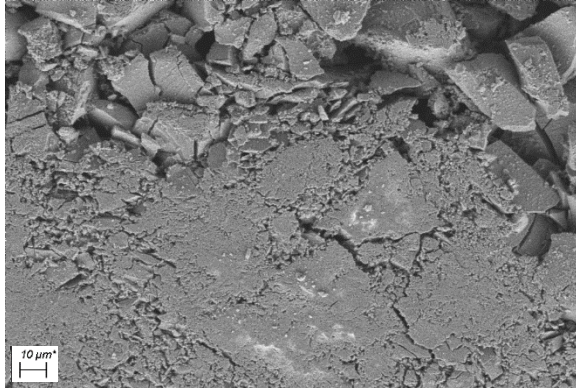
$x_{\text{Seeds}} = 0$ w%: $x_{\text{Seeds}} = 3$ w%:
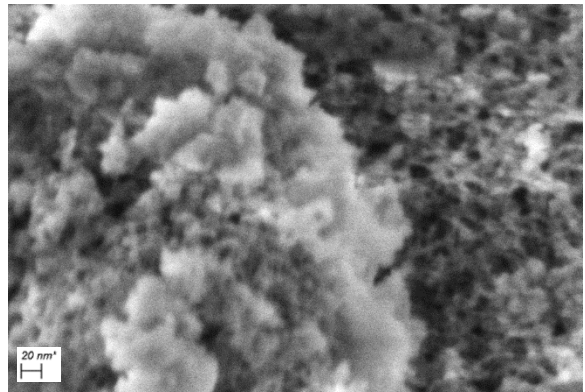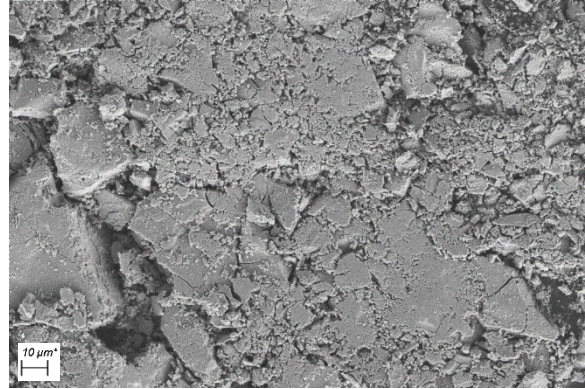
Figure 13. SEM images of two aged precursor from an unseeded (left) and seeded (right) aging, respectively, at two magnifications.

Table 1. Selected $t_{\text{change,pH}}$ and physicochemical properties of the aged precursors and precatalysts from unseeded and seeded experiments for two initial pH. Values missing due to limited resources are indicated by 'n.a.'.

Precatalyst	$t_{\text{change,pH}}$ [min]	$\tilde{x}_{\text{Cu,metals}}$ [mol%]	$\tilde{x}_{\text{Zn,metals}}$ [mol%]	$\tilde{x}_{\text{Zr,metals}}$ [mol%]	S_{BET} [m$^2 \cdot$g^{-1}]	$\bar{d}_{\text{Pore,BJH}}$ [nm]	$d_{\text{CuO,XRD}}$ [nm]
$pH(0\text{ min}) = 6.7$ $x_{\text{Seeds}} = 0$ w%	96 ± 5	59.1; 60.2; 61.9; 64.1	32.4; 31.8; 29.2; 28.1	8.5; 8.0; 7.1; 7.7	117; 120; 125	9.2; 9.2; 11.2	2.9 ± 0.8
$pH(0\text{ min}) = 6.7$ $x_{\text{Seeds}} = 3$ w%	53; 57	59.1	32.1	8.7	122; 124	9.2; 9.2	3.0; 3.7
$pH(0\text{ min}) = 6.7$ $x_{\text{Seeds}} = 8$ w%	(69.4)	63.7	28.0	8.1	n.a.	n.a.	1.7
$pH(0\text{ min}) = 6.7$ $x_{\text{Seeds}} = 27$ w%	12.5; 14.7	64.3	28.4	7.2	n.a.	n.a.	1.7; 2.0
$pH(0\text{ min}) = 7.1$ $x_{\text{Seeds}} = 0$ w%	72.4; 79.9	60.2	31.8	8.0	104; 107	9.2; 11.2	4.1; 4.3
$pH(0\text{ min}) = 7.1$ $x_{\text{Seeds}} = 3$ w%	36.0; 40.1	n.a.	n.a.	n.a.	94; 103	9.2; 9.2	4.0; 4.6

The molar fractions of Cu, Zn and Zr, analyzed on the aged precursor, are consistent in between samples with different x_{Seeds} as are the mass specific surface areas and the pore sizes which were respectively characterized by N$_2$ physisorption on the precatalyst. Compared to S_{BET} and $\bar{d}_{\text{Pore,BJH}}$ of other Cu/Zn/Zr based precatalysts in literature [10,13], the values are

well within the expected range. This confirms the assumption from the SEM images that seeding does not affect the microstructure. For both initial pH no influence of x_Seeds on the CuO crystallite size determined by Rietveld refinement is evident.

Overall, the results show that aging time at liter scale can be reduced significantly by seeding without altering the considered properties of the aged precursor and the precatalyst. Thus, the nanostructure seems to remain unchanged. Higher x_Seeds lead to increasingly short turnover times in aging. In general, the activitiy, selectivity and longevity of a Cu/Zn based catalyst are correlated to the fraction of zincian malachite after aging as well as S_BET, the metal fractions and the pore size of its precatalyst [10,16,23]. Thus, if these properties remain unchanged, the catalyst quality should accordingly remain unchanged. Nevertheless, a comparison of catalysts from an unseeded and a seeded aging in a MeOH synthesis is strongly recommended to confirm that both methods deliver equivalent catalysts.

5 Conclusions

The focus of this study was on the aging step in the preparation of Cu/Zn based catalysts for the MeOH synthesis with a twofold objective. For one thing, it was to be resolved if aging can be understood as a thermodynamic equilibrium process and thus the solids phase composition after aging could be predicted using a thermodynamic model which might be useful when adapting the preparation to new requirements on the catalyst. On the other hand, seeding as a potential method to accelerate aging and thus enhancing process control and reducing energy consumption while maintaining the same product qualities was to be evaluated.

The thermodynamic model consists of two components: an activity coefficient model, which may consider ion association by complex formation in addition to ion interaction, and a compilation of solubility products of the solids phases relevant for aging $K_{\text{SP},j}$. A comparison of four activity coefficient models comparing measured and calculated pH values of the reactants revealed that the ion interaction in the $NaHCO_3$ reactant solution up to $I = 6\,\text{mol} \cdot (\text{kg H}_2\text{O})^{-1}$ can be described with deviations of less than 5 % even by more simple models, e.g. the Davies extended Debye-Hückel equation. In contrast, only a more complex model, here the Pitzer model, allowed to correctly depict the speciation of the $Cu(NO_3)_2/Zn(NO_3)_2$ solution up to $I = 12\,\text{mol} \cdot (\text{kg H}_2\text{O})^{-1}$, however with errors of up to 15 %. Values for $K_{\text{SP},j}$ were taken from mineral phases in the literature. The thermodynamic model was able to depict the general influence of the Cu/Zn ratio as well as the pH on the solids phase composition and the molar Zn fraction in zincian malachite after aging. However, a quantitative comparison does show significant deviations between model and measurement in the transition area between zincian malachite predominance and aurichalcite predominance. Also, the temperature dependency cannot be accurately modelled using only literature data. It is strongly recommended to fit existing data to the shown properties of the synthetic phases or to experimentally determine $K_{\text{SP},j}$ for these phases in the future to improve the model quality. For future Rietveld refinements the use of a single aurichalcite phase with a variable Cu fraction between 0 and approx. 40 mol% and corresponding variable lattice parameters similar to the procedure chosen for zincian malachite may prove beneficial for even more precise phase compositions.

A study by Güldenpfennig et al. [30] showed that seeding does influence the aging kinetics at microliter scale. Based on that study, we quantitatively examined the influence of seeding on aging kinetics at liter scale for more process conditions, higher concentrations and in regard to the influence on the physicochemical properties of the aged precursor and the precatalyst. Comparative studies for two different initial pH showed that necessary aging times can be reduced by 43 % to 50 % by adding a seeding mass fraction of just $x_\text{Seeds} = 3\,\text{w\%}$. pH minima, color changes and phase compositions determined by XRD measurements were used and compared as indicators to show a completed phase transformation during aging. A further increase of x_Seeds leads to progressively shorter process times necessary to complete phase

change down to a minimum of 8 min for $x_{\text{Seeds}} = 42$ w% instead of 96 min.

A comparison of the metallic and phase composition as well as the morphology of the aged precursors from unseeded and seeded experiments showed no differences. Furthermore, the mass specific surface area S_{BET}, the mean pore size $\bar{d}_{\text{Pore,BJH}}$, the CuO crystallite size $d_{\text{CuO,XRD}}$ and the phase composition of the precatalysts also seem to be independent from the seeding mass fraction used in aging. Only a comparison of FT-IR spectra of unseeded and seeded samples hints at a possible accumulation of aurichalcite in the aged precursor when using seeds. In total, the almost unchanged properties of the aged precursor and the precatalyst for different x_{Seeds} indicate that seeding accelerates aging significantly without altering the qualities of the final catalyst which correlate with the analyzed physicochemical properties.

Our next step is to compare catalysts from an unseeded and a seeded aging in a MeOH synthesis to confirm that seeding does not influence the catalyst properties negatively. If the catalyst prepared by seeded aging proves adequately operational, seeding experiments at the industrial scale are advisable to ensure the applicability of the findings of this work on the necessary scale. Complementary studies at lab scale on the influence of total solids weight fraction in the aging suspension, even higher seeding mass fractions and repeated seeding on the aging kinetics and resulting physicochemical properties of the aged precursor should be performed to conclusively evaluate the great potential of seeding for process control and economic optimization of aging.

Acknowledgements

Symbols used

a	[-]	activity
a_{zM}	[Å]	lattice parameter of zincian malachite
b	[mol· (kg H_2O)$^{-1}$]	molality
b^0	[mol· (kg H_2O)$^{-1}$]	reference molality; $1\ \text{mol} \cdot \text{kg}^{-1}$
b_{zM}	[Å]	lattice parameter of zincian malachite
c_{zM}	[Å]	lattice parameter of zincian malachite
d	[nm]	particle/ pore size
d_{stirrer}	[mm]	diameter
I	[mol· (kg H_2O)$^{-1}$]	ionic strength
K_{IA}	[-]	ion association product
K_{SP}	[-]	solubility product
m	[kg]	mass
n	[mol]	amount of substance
pH	[-]	pH value
R	[J·K^{-1}·mol^{-1}]	gas constant
R^2	[-]	coefficient of determination
S	[-]	supersaturation
S_{BET}	[m^2·g^{-1}]	mass-specific surface area
T	[°C]	temperature
t_{Age}	[min]	aging time
V	[m^3]	volume
X	[mL·L^{-1}]	volumetric load

x	[w%]	mass fraction
$\tilde{x}$	[mol%]	molar fraction
Y	[kg·L⁻¹]	yield

Greek letters

β_{zM}	[°]	lattice parameter of zincian malachite
$\Delta_r H^0$	[J·mol⁻¹]	standard reaction enthalpy
ΔY	[kg·L⁻¹]	corrected yield (deducting the seeding mass)
γ	[-]	activity coefficient
ν	[-]	stoichiometric coefficient
$\tilde{\nu}$	[cm⁻¹]	wavenumber
σ	[mol%]	standard deviation
θ	[°]	scattering angle
χ^2	[-]	Error in Rietveld refinement

Sub- and Superscripts

±	all ions of a salt
*	at thermodynamic equilibrium
0	standard conditions
age	aging time; starting when co-precipitation is completed
Aur	aurichalcite
BET	determined by the Brunnauer-Emmett-Teller model
BJH	determined by the Barett-Joyner-Halenda method
change	turnover point in aging indicating a phase change
End	Final state
i	solids-forming ion
j	solid phase
k	complex/ ion associate
metals	in relation to the total metal content
pH	determined by local pH minimum
phase	solid phase
XRD	determined by XRD/ Rietveld refinement
zM	zincian malachite

Abbreviations

BET	Brunnauer-Emmett-Teller model
BJH	Barett-Joyner-Halenda method
EDXS	energy-dispersive X-ray spectroscopy
ICP-OES	inductively coupled plasma optical emission spectrometry
FT-IR	Fourier-transform infrared spectroscopy
MeOH	methanol
SEM	scanning electron microscopy
XRD	X-ray diffraction
XRF	X-ray fluorescence spectroscopy

References

[1] D. E. Brown, T. Edmonds, R. W. Joyner, J. J. McCarroll, S. R. Tennison, *Catal Lett (4)*, *144*, 545ff, (2014).

[2] G. A. Olah, *Angewandte Chemie (International ed. in English) (18)*, *44*, 2636ff, (2005).

[3] M. Bjørgen, F. Joensen, M. Spangsberg Holm, U. Olsbye, K.-P. Lillerud, S. Svelle, *Applied Catalysis A: General (1)*, *345*, 43ff, (2008).

[4] M. Behrens, F. Studt, I. Kasatkin, S. Kühl, M. Hävecker, F. Abild-Pedersen, S. Zander, F. Girgsdies, P. Kurr, B.-L. Kniep, M. Tovar, R. W. Fischer, J. K. Nørskov, R. Schlögl, *Science (New York, N.Y.) (6083)*, *336*, 893ff, (2012).

[5] F. Arena, K. Barbera, G. Italiano, G. Bonura, L. Spadaro, F. Frusteri, *Journal of Catalysis (2)*, *249*, 185ff, (2007).

[6] A. Sternberg, A. Bardow, *ACS Sustainable Chem. Eng. (8)*, *4*, 4156ff, (2016).

[7] C. Baltes, S. Vukojevic, F. Schuth, *Journal of Catalysis (2)*, *258*, 334ff, (2008).

[8] Y. Choi, K. Futagami, T. Fujitani, J. Nakamura, *Applied Catalysis A: General (1-2)*, *208*, 163ff, (2001).

[9] S. Kuld, M. Thorhauge, H. Falsig, C. F. Elkjær, S. Helveg, I. Chorkendorff, J. Sehested, *Science (New York, N.Y.) (6288)*, *352*, 969ff, (2016).

[10] S. Polierer, D. Guse, S. Wild, K. Herrera Delgado, T. N. Otto, T. A. Zevaco, M. Kind, J. Sauer, F. Studt, S. Pitter, *Catalysts (8)*, *10*, 816ff, (2020).

[11] F. Arena, G. Italiano, K. Barbera, S. Bordiga, G. Bonura, L. Spadaro, F. Frusteri, *Applied Catalysis A: General (1)*, *350*, 16ff, (2008).

[12] S. Wild, S. Polierer, T. A. Zevaco, D. Guse, M. Kind, S. Pitter, K. Herrera Delgado, J. Sauer, *RSC Adv. (5)*, *11*, 2556ff, (2021).

[13] D. Guse, S. Polierer, S. Wild, S. Pitter, M. Kind, *Chemie Ingenieur Technik 94, 3*, 314ff, (2022).

[14] B. Bems, M. Schur, A. Dassenoy, H. Junkes, D. Herein, R. Schlögl, *Chemistry*, *9*, 2039ff, (2003).

[15] A. M. Pollard, M. S. Spencer, R. G. Thomas, P. A. Williams, J. Holt, J. R. Jennings, *Applied Catalysis A: General (1)*, *85*, 1ff, (1992).

[16] M. Behrens, R. Schlögl, *Z. anorg. allg. Chem. (15)*, *639*, 2683ff, (2013).

[17] D. M. Whittle, A. A. Mirzaei, J. S. J. Hargreaves, R. W. Joyner, C. J. Kiely, S. H. Taylor, G. J. Hutchings, *Phys. Chem. Chem. Phys. (23)*, *4*, 5915ff, (2002).

[18] T. Fujitani, J. Nakamura, *Applied Catalysis A: General*, *191*, 111ff, (2000).

[19] M. S. Spencer, *Topics in Catalysis*, *8*, 259ff, (1999).

[20] X. Jiang, L. Zheng, Z. Wang, J. Lu, *Journal of Molecular Catalysis A: Chemical*, *423*, 457ff, (2016).

[21] X. Jiang, X. Qin, C. Ling, Z. Wang, J. Lu, *AIChE J. (2-3)*, *124*, 123ff, (2018).

[22] Q.-C. Zhang, K.-P. Cheng, L.-X. Wen, K. Guo, J.-F. Chen, *RSC Adv. (40)*, *6*, 33611ff, (2016).

[23] N. Mota, R. Guil-Lopez, B. G. Pawelec, J. L. G. Fierro, R. M. Navarro, *RSC Adv. (37)*, *8*, 20619ff, (2018).

[24] T. Fujitani, J. Nakamura, *Catal Lett (2/3)*, *56*, 119ff, (1998).

[25] P. J. Smith, S. A. Kondrat, P. A. Chater, B. R. Yeo, G. M. Shaw, L. Lu, J. K. Bartley, S. H. Taylor, M. S. Spencer, C. J. Kiely, G. J. Kelly, C. W. Park, G. J. Hutchings, *Chemical science (3)*, *8*, 2436ff, (2017).

[26] G. Sengupta, D. P. Das, M. L. Kundu, S. Dutta, S. K. Roy, R. N. Sahay, K. K. Mishra, S. V. Ketchik, *Applied Catalysis (1)*, *55*, 165ff, (1989).

[27] S. Kaluza, M. Behrens, N. Schiefenhövel, B. Kniep, R. Fischer, R. Schlögl, M. Muhler, *ChemCatChem (1)*, *3*, 189ff, (2011).

[28] M. Behrens, *Journal of Catalysis (1)*, *267*, 24ff, (2009).

[29] J. Schumann, T. Lunkenbein, A. Tarasov, N. Thomas, R. Schlögl, M. Behrens, *ChemCatChem (10)*, *6*, 2889ff, (2014).

[30] A. Güldenpfennig, M. Distaso, W. Peukert, *Chemical Engineering Journal*, *369*, 996ff, (2019).

[31] F. Liao, Y. Huang, J. Ge, W. Zheng, K. Tedsree, P. Collier, X. Hong, S. C. Tsang, *Angewandte Chemie (9)*, *50*, 2162ff, (2011).

[32] D. R. Palo, R. A. Dagle, J. D. Holladay, *Chem. Rev. (10)*, *107*, 3992ff, (2007).

[33] S. Tada, K. Larmier, R. Büchel, C. Copéret, *Catal. Sci. Technol. (8)*, *8*, 2056ff, (2018).

[34] R. Ahmad, M. Hellinger, M. Buchholz, H. Sezen, L. Gharnati, C. Wöll, J. Sauer, M. Döring, J.-D. Grunwaldt, U. Arnold, *Catalysis Communications*, *43*, 52ff, (2014).

[35] M. Behrens, F. Girgsdies, *Z. anorg. allg. Chem. (6)*, *636*, 919ff, (2010).

[36] L. Zwiener, F. Girgsdies, D. Brennecke, D. Teschner, A. G. Machoke, R. Schlögl, E. Frei, *Applied Catalysis B: Environmental*, *249*, 218ff, (2019).

[37] M. Behrens, F. Girgsdies, A. Trunschke, R. Schlögl, *Eur. J. Inorg. Chem. (10)*, *2009*, 1347ff, (2009).

[38] N. Perchiazzi, *Z. Kristallogr. Suppl. 23*, 505ff, (2006).

[39] B. Fehér, S. Szakáll, S. Bigi, *2nd Central-European Mineralogical Conference. Mineralogia - Special Papers 32*, (2008).

[40] B. Fehér, S. Szakáll, N. Zajzon, J. Mihály, *Miner Petrol (4)*, *109*, 405ff, (2015).

[41]   N. Perchiazzi, N. Demitri, B. Fehér, P. Vignola, *Can Mineral (6)*, *55*, 1027ff, (2017).
[42]   M. A. Hartig, N. Jacobsen, W. Peukert, *Chemical Engineering Science*, *109*, 158ff, (2014).
[43]   M. A. J. Hartig, W. Peukert, N. Jacobsen, A. Leuthold, *AIChE J. (7)*, *61*, 2104ff, (2015).
[44]   M. Haderlein, A. Güldenpfennig, D. Segets, W. Peukert, *Computers & Chemical Engineering*, *98*, 197ff, (2017).
[45]   A. S. Myerson, *Handbook of industrial crystallization*, 2nd edn, (2002).
[46]   J.W. Mullin, *Crystallization*, 4th edn, (2001).
[47]   J. Manuel García-Ruiz, *Journal of structural biology (1)*, *142*, 22ff, (2003).
[48]   W. Beckmann, *Crystallization: Basic concepts and industrial applications,* (2013).
[49]   T. L. Threlfall, R. W. De'Ath, S. J. Coles, *Org. Process Res. Dev. (3)*, *17*, 578ff, (2013).
[50]   T. L. Threlfall, S. J. Coles, *CrystEngComm (3)*, *18*, 369ff, (2016).
[51]   M. Barros Groß, M. Kind, Crystal Growth & Design (6), 17, 3491ff, (2017).
[52]   F.M.M. Morel, J. G. Hering, *Principles and applications of aquatic chemistry*, (1993).
[53]   A. H. Truesdell, B. F. Jones, *Journal of Research of the U.S. Geological Survey (2)*, *2*, 233ff, (1974).
[54]   K. S. Pitzer, G. Mayorga, *J. Phys. Chem. (19)*, *77*, 2300ff, (1973).
[55]   K. S. Pitzer, G. Mayorga, *J Solution Chem (7)*, *3*, 539ff, (1974).
[56]   A. Lassin, C. Christov, L. Andre, M. Azaroual, *American Journal of Science (3)*, *315*, 204ff, (2015).
[57]   K. J. Powell, P. L. Brown, R. H. Byrne, T. Gajda, G. Hefter, S. Sjöberg, H. Wanner, *Pure and Applied Chemistry (5)*, *79*, 895ff, (2007).
[58]   A. K. Alwan, J. H. Thomas, P. A. Williams, *Transition Metal Chemistry (1)*, *5*, 3ff, (1980).
[59]   W. Preis, H. Gamsjäger, *The Journal of Chemical Thermodynamics (7)*, *33*, 803ff, (2001).
[60]   E. Giffaut, M. Grivé, P. Blanc, P. Vieillard, E. Colàs, H. Gailhanou, S. Gaboreau, N. Marty, B. Madé, L. Duro, *Applied Geochemistry*, *49*, 225ff, (2014).
[61]   N. Doebelin, R. Kleeberg, *J Appl Crystallogr (Pt 5)*, *48*, 1573ff, (2015).
[62]   S. Klokishner, M. Behrens, O. Reu, G. Tzolova-Müller, F. Girgsdies, A. Trunschke, R. Schlögl, *The journal of physical chemistry. A (35)*, *115*, 9954ff, (2011).
[63]   S. Zander, B. Seidlhofer, M. Behrens, *Dalton transactions (43)*, *41*, 13413ff, (2012).
[64]   S. A. Kondrat, P. J. Smith, P. P. Wells, P. A. Chater, J. H. Carter, D. J. Morgan, E. M. Fiordaliso, J. B. Wagner, T. E. Davies, L. Lu, J. K. Bartley, S. H. Taylor, M. S. Spencer, C. J. Kiely, G. J. Kelly, C. W. Park, M. J. Rosseinsky, G. J. Hutchings, *Nature (7592)*, *531*, 83ff, (2016).
[65]   D. Stoilova, V. Koleva, V. Vassileva, *Spectrochimica Acta Part A: Molecular and Biomolecular Spectroscopy (9)*, *58*, 2051ff, (2002).